















A geological carbon cycle sink hosted by ocean crust talus breccias

Received: 13 March 2024

Accepted: 1 October 2025

Published online: 24 November 2025

 Check for updates

Rosalind M. Coggon ^{1,15} ✉, Elliot J. Carter ^{2,15}, Lewis J. C. Grant^{1,15}, Aled D. Evans ^{1,15}, Christopher M. Lowery³, Damon A. H. Teagle ¹, Pamela D. Kempton ⁴, Matthew J. Cooper ¹, Claire M. Routledge ⁵, Elmar Albers ⁶, Justin Estep ⁷, Gail L. Christeson ⁸, Michelle Harris ⁹, Thomas M. Belgrano¹⁰, Jason B. Sylvan ¹¹, Julia S. Reece ¹², Emily R. Estes^{13,14} & Trevor Williams ¹³ on behalf of The South Atlantic Transect IODP Expedition 390 & 393 Scientists*

Calcium carbonate precipitation in ageing ocean crust sequesters carbon dioxide dissolved in seawater through seafloor weathering reactions, influencing atmospheric CO₂ concentrations on million-year timescales. However, this crustal carbon sink, and the extent it balances CO₂ degassing during crustal formation at mid-ocean ridges, remain poorly quantified due to limited sampling of the vast ridge flanks where CO₂ uptake continues for millions of years. Here we quantify the carbon sink hosted within talus breccias that accumulated through mass wasting 61 million years ago during rift faulting at the slow spreading Mid-Atlantic Ridge, cored during International Ocean Discovery Program South Atlantic Transect Expedition 390. After 40 million years of carbonate cementation, these breccias contain ~7.5 wt% seawater-derived CO₂, 2 to 40 times more than previously cored upper crust. Our estimates of talus breccia abundance based on fault geometries indicate that talus formed at slow-spreading ridges can accommodate a CO₂ sink equivalent to a large proportion of the CO₂ released during accretion of the underlying crust. The proportion of plate divergence accommodated by faulting, and hence talus abundance, increases nonlinearly with decreasing spreading rate. Consequently, past variations in spreading rate may have impacted the balance between ocean crust CO₂ release and uptake in Earth's carbon cycle.

The formation of new ocean crust at mid-ocean ridges (MORs), its subsequent ageing over millions of years as it traverses the ocean basins and eventual subduction into the mantle is an integral component of the geological carbon cycle. Basaltic magma degassing during MOR volcanism releases large volumes of CO₂ to the oceans and atmosphere, with the modern global flux estimated to be $1.32^{+0.77}_{-0.85} \times 10^{12}$ mol yr⁻¹ (ref. 1). Subsequent precipitation of calcium carbonate (CaCO₃) minerals during circulation of seawater-derived hydrothermal fluids through the ocean crust sequesters CO₂, which

is transported towards subduction zones as the crust ages²⁻⁴. This carbon sink can be quantified from sections of hydrothermally altered ocean crust that provide time-integrated records of their geochemical exchanges with hydrothermal fluids. The fluxes of CO₂ from and to the ocean crust remain poorly quantified but are often assumed to be in balance⁵, although evidence suggests they are not^{2,6-8}. Whether the formation and evolution of the ocean crust influenced past atmospheric CO₂ concentrations, and hence climate, remains debated^{2-5,8,9}, principally due to imprecise knowledge of the conditions, extent,

A full list of affiliations appears at the end of the paper. ✉ e-mail: R.M.Coggon@soton.ac.uk

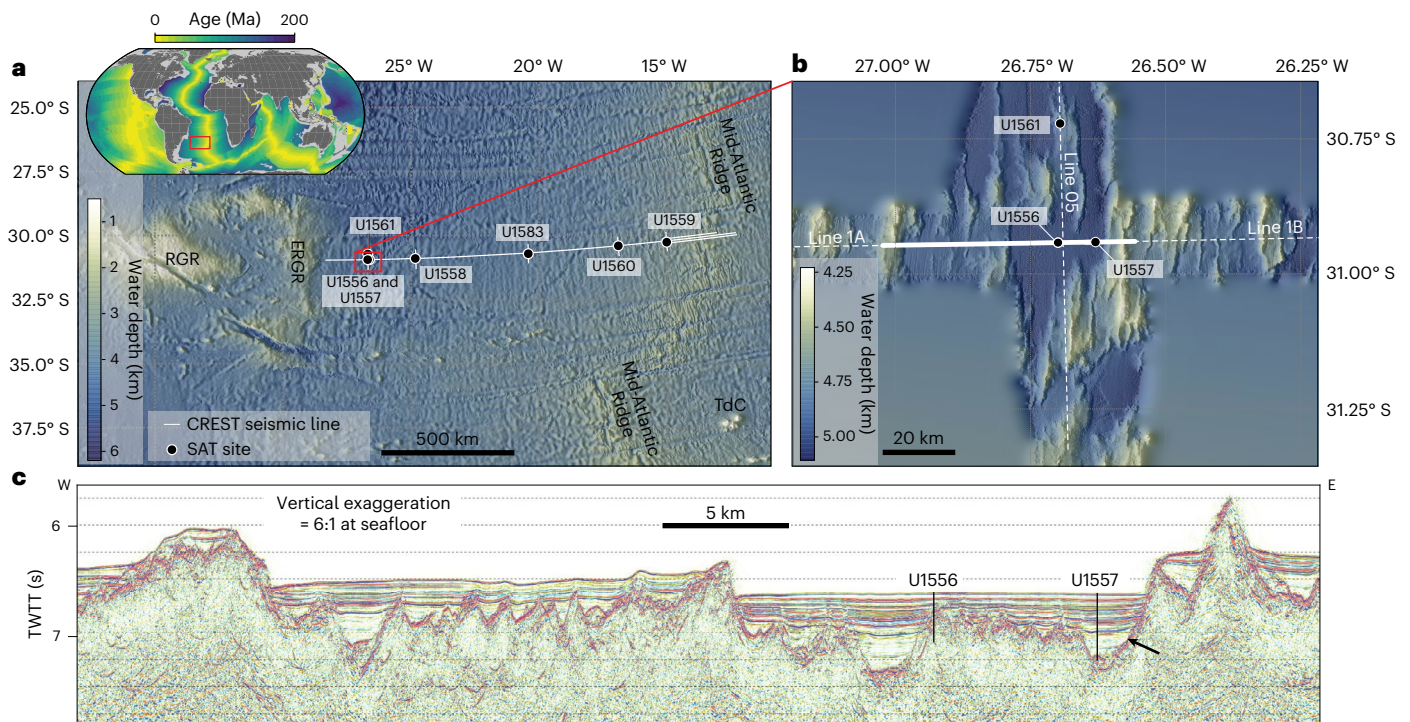


Fig. 1 | Location and tectonic setting of the SAT drill sites. **a**, Bathymetry⁴⁷ of SAT area in the South Atlantic Ocean (adapted from ref. 17), showing the locations of the SAT drill sites (black circles); inset shows the location of the SAT area on a map of sea floor age⁴⁸. **b**, Bathymetry⁴⁷ of the -61-Ma SAT study area, where sites U1557 and U1556 are located in the same sediment-filled basin¹⁷. White lines, CREST seismic reflection profiles⁴⁹; RGR, Rio Grande Rise; ERGR, eastern Rio Grande Rise; TdC, Tristan de Cunha. **c**, CREST seismic reflection profile⁴⁹, parallel to the SAT, showing the locations of SAT Site U1557 adjacent to a Mid-Atlantic

Ridge-parallel fault and Site U1556 on the adjacent faulted basement high; portion of the CREST line shown indicated by the solid white line in the study area map **b**. Black arrow indicates the sediment–basement interface. TWTT, two-way travel time. The sediment-free, or thinly sedimented, exposed basement ridges -15 km west and -5 km east of Site U1557 allow fluids in and out of the basement, with lateral channelling through the basement between these outcrops likely, as observed through upper crustal aquifers elsewhere^{50,51}.

depth and duration of hydrothermal CaCO_3 precipitation within the ageing ridge flanks.

Given their vast extent globally, the hydrothermal fluid flux through ridge flanks is many orders of magnitude greater than that through high-temperature ($\leq 400^\circ\text{C}$) axial systems¹⁰. Conductive heat-flow studies indicate advection of heat by low-temperature ($<100^\circ\text{C}$) hydrothermal fluids persists across ridge flanks for 65 Myr on average (for example, refs. 11–13). However, fluid flow can occur at any crustal age given sufficient hydrologic driving forces. The extent and duration of ridge flank fluid flow are therefore affected by various parameters including basement topography, volcanic stratigraphy and lava morphology, the extent to which hydrothermally sealed fractures (veins) are re-cracked and the composition, thickness and completeness of sediment cover (for example, refs. 14–16), many of which are strongly influenced by spreading rate. Scientific ocean drilling provides the only means to sample ocean crust across the sedimented ridge flanks. However, due to unrepresentative sampling of upper ocean crust with respect to basement age, spreading rate and sediment thickness^{17,18}, there was a dearth of drill core from middle-aged (20–100 Ma) and slow-spread crust through which heat-flow studies and crustal architecture suggest prolonged circulation of seawater should occur on ridge flanks.

Newly acquired cores of 7 to 61 Ma slow-spread crust drilled in the western South Atlantic along the South Atlantic Transect (SAT) during International Ocean Discovery Program (IODP) Expeditions 390 C, 395E, 390 and 393 provide a unique opportunity to understand the role of ageing ocean crust in long-term biogeochemical cycles and the influence of spreading rate on hydrothermal alteration through comparison with other well-characterized sites¹⁷. Carbonate-cemented talus breccia cores from IODP Site U1557, located on 60.7-Ma crust

on the western flank of the southern Mid-Atlantic Ridge, represent a previously underappreciated sink in the global carbon cycle hosted by slow-spread crust. This sink occurs as a direct consequence of the impact of slow-spreading rates on crustal architecture.

At slow-spreading ridges $>10\%$ of the plate divergence is accommodated by tectonic strain through normal faulting, resulting in a well-defined axial valley 0.8–1.6-km deep and 5–25-km wide (for example, refs. 19–22). The relief, slopes and seismicity of the normal fault scarps promote erosion and mass wasting, resulting in accumulation of porous basaltic talus breccias against the axial valley walls^{23,24}. These faults remain active as the crust spreads away from the axis resulting in rough horst and graben basement topography on the ridge flanks²⁵. Coring at Site U1557 recovered the first talus breccias from a middle-aged slow-spreading ridge flank, revealing that through carbonate precipitation and cementation over tens of millions of years, these clastic deposits sequester large quantities of dissolved seawater carbon. Here we describe the hydrothermal cementation of Site U1557 talus breccias, quantify their CO_2 uptake over at least 40 million years and extrapolate these observations to estimate the carbon sink that talus breccias on slow-spread crust may constitute.

SAT crustal architecture

The SAT drilling recovered complete sedimentary sections and up to 340 m of the underlying oceanic crust along a crustal flowline across the western flank of the slow- to intermediate-spreading ($13\text{--}31\text{ mm yr}^{-1}$ half rate²⁶) Mid-Atlantic Ridge at $\sim 31^\circ\text{S}$ (ref. 17) (Fig. 1). Before drilling, the Crustal Reflectivity Experiment Southern Transect (CREST) conducted a detailed geophysical survey of crust formed 0–70 million years ago (Ma) along the -1,400 km SAT crustal flowline^{26–28}.

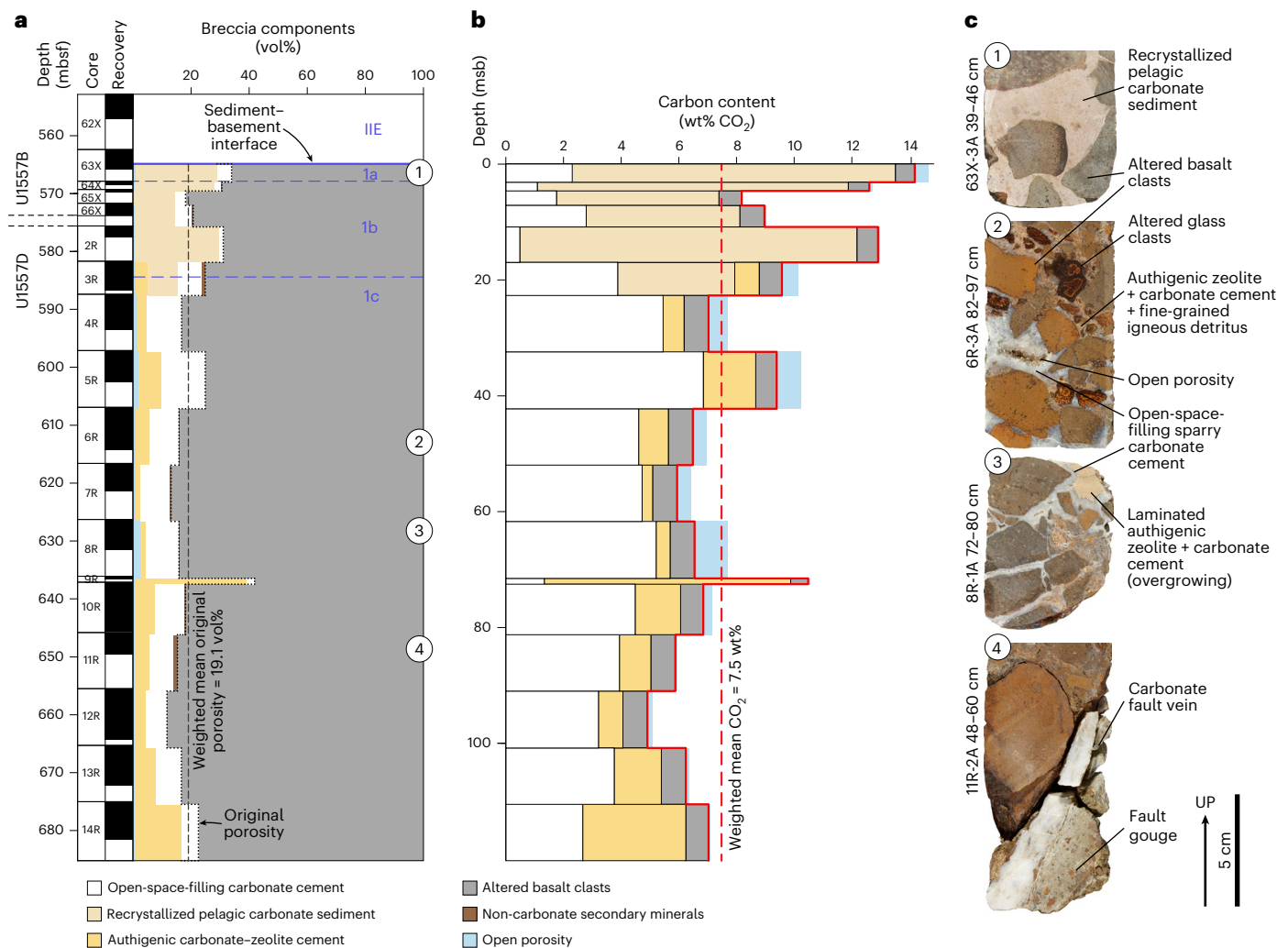


Fig. 2 | Site U1557 talus breccia stratigraphy and carbon content. **a**, Composite U1557 stratigraphy, comprising Holes U1557B and U1557D, showing the variations in abundance (vol%) of breccia components downhole. Depth is given in both metres below seafloor (mbsf) and metres sub-basement (msb). Black bars indicate degree of recovery in each core interval. The solid blue line indicates the sediment–basement interface, and dashed blue lines and numbers indicate lithological subunits. The original porosity is outlined with black dots and the mean total original porosity of the cored deposit, weighted by core interval lengths to normalize to core recovery (Supplementary Table 1), is indicated by the dashed black line. Numbers in circles indicate the depths of core photographs in **c**. **b**, Total carbon content (wt% CO₂) of each core (solid red line), calculated from the

CO₂ concentrations, volume proportions and densities of the carbonate-bearing components, following equation (2), with the contribution of each breccia component indicated by the coloured bars. The mean CO₂ content of the breccia, weighted by core interval lengths to normalize to core recovery (Supplementary Table 1), is indicated by the red dashed line. Blue bars indicate the additional CO₂ capacity of the breccia, if all open porosity was filled with CaCO₃ cement.

c, Photographs of selected core pieces¹⁷ illustrating key features: (1) altered basalt clasts in a recrystallized pelagic carbonate sediment matrix; (2) typical carbonate-cemented breccia; (3) breccia with authigenic zeolite + carbonate cement overgrowing sparry carbonate cement; (4) carbonate fault vein cutting through breccia at high angle and underlain by fine-grained greenish fault gouge.

Seismic imaging revealed a well-developed ridge–basin seafloor texture outside the normal fault-bounded axial valley, comprising sediment-filled fault-bounded basins (up to ~650-m deep and 2–4 km across) sub-parallel to the ridge axis and common small seamounts²⁷. Sediment-free or thinly sedimented exposed basement outcrops that may allow seawater and ridge flank hydrothermal fluids to flow in and out of the crust are abundant along the CREST survey line (for example, Fig. 1c). As the crust is never fully sealed by sediment²⁸, there may be long-lived (>65 Myr) and ongoing connection between the ocean and uppermost crust. This rough topography contrasts with reference sections of faster-spread ocean crust that have been the focus of investigation in recent decades, where high sedimentation rates (for example, refs. 29,30) promoted sealing of the crust from the ocean leading to anomalously high basement temperatures and earlier cessation of hydrothermal circulation³¹.

Site U1557 carbonate-cemented talus breccias

Given considerable variations in sediment thickness and continuity along the SAT^{26,27}, Expedition 390 occupied two sites on ~61-Ma crust to investigate the variability in duration and extent of hydrothermal alteration due to rugged basement topography at a given crustal age. The 61.2-Ma crust at Site U1556 is overlain by ~278 m of sediment, whereas Site U1557, ~6.5 km to the east, is located on 60.7-Ma crust in a more thickly sedimented (~564 m) portion of the same local sediment basin¹⁷ (Fig. 1). The upper basement cored at U1556 comprises a ~340-m volcanic sequence of pillow lavas, hyaloclastite breccias and massive flows typical of slow-spread crust. In contrast, at Site U1557 the upper basement comprises a basaltic talus breccia deposit, with Hole U1557B capturing the sediment–basement interface and Hole U1557D penetrating 120 m into the deposit, without reaching intact lavas (Fig. 2). The talus is interpreted to have formed against the

adjacent uplifted basement fault block¹⁷. Middle Palaeocene planktic foraminifera and calcareous nannoplankton in the sediments directly overlying the breccia are indicative of Zones P4a (60.54–60.76 Ma) and CNP7 (60.76–61.17 Ma), respectively^{17,32}, indicating the breccia accumulated soon after accretion of the underlying lavas, probably during uplift on axial valley wall bounding faults.

The U1557 breccia is largely clast supported, comprising centimetre-scale fragments of pillow basalt displaying a range of pre- and post-brecciation alteration styles and millimetre- to centimetre-scale fragments of altered volcanic glass. Between these clasts was considerable primary porosity equivalent to ~12–42 vol% of the recovered cores, averaging >19 vol% (Fig. 2 and Supplementary Table 1). Consequently, the breccia deposit had high interconnected porosity with a large surface area for fluid–rock reaction and substantial accommodation space for hydrothermal precipitates. This macropore space is now variably filled by sparry carbonate cement, fine-grained clastic volcanic material, microcrystalline authigenic zeolite + carbonate cement and/or pelagic sediment, with millimetre- to centimetre-scale open porosity still common throughout much of the core (<2.4 vol%; Fig. 2).

Despite the rubbly nature of the original talus pile, there was good core recovery (averaging 63%; Fig. 2 and Supplementary Table 1). Individual core pieces <122 cm long and a maximum core recovery of 97%, despite comprising centimetre-scale basaltic clasts, reflect the robustness of hydrothermal cementation. Sparry calcite cement is ubiquitous, typically growing into open space, with a dog-toothed habit. Sparry calcite growths covering the ends of many core pieces indicate there are voids wider than the 6-cm diameter core, and consequently, the in situ formation-scale porosity is probably underestimated based on description of recovered material alone. In the lower part of the cored hole (>75 metres sub-basement; msb), calcite cements have a sugary texture, and the remnant porosity is lower¹⁷. Altogether, these open-space-filling carbonate cements make up 1.1 to 14.6 vol% of the recovered cores with a mean abundance of 8.7 ± 3.2 vol% ($\pm 1\sigma$), weighted by core interval lengths to normalize for variable core recovery (Fig. 2 and Supplementary Table 1).

Low-temperature hydrothermal alteration of the basaltic breccia clasts is also ubiquitous, manifest in the formation of secondary minerals, which include calcite in addition to clays, iron oxyhydroxides and zeolite. These carbonate-bearing assemblages replace olivine and plagioclase phenocrysts and groundmass, and fill vesicles and fractures to form veins¹⁷.

In the uppermost breccia cores, from immediately below the sediment–basement interface, buff to pale peach recrystallized microfossil-bearing pelagic sediments form the breccia matrix and crystalline cement is rare. Pelagic sediment is absent deeper than ~20 m into the breccia, but a microcrystalline cement similar in appearance to the sediment matrix is ubiquitous below this depth. This cement comprises an authigenic mixture of phillipsite zeolite and carbonate, providing an additional hydrothermal carbon sink component within the breccia.

We calculated the CO₂ content of the U1557 talus breccia from the measured carbon concentrations of its carbonate-bearing components, their respective volume proportions of the recovered cores, and their densities (Supplementary Tables 1 and 2). The CO₂ contents of individual cores range from 4.9 to 14.1 wt%, yielding an average bulk breccia deposit CO₂ content of 7.5 ± 2.2 wt%, weighted by core interval lengths to normalize for variable core recovery (Methods and Supplementary Table 1). Previously cored upper ocean crust contains 0.2 to 4.2 wt% CO₂, with Mesozoic crust typically having higher CO₂ contents than Cenozoic crust and slow-spread crust containing more CO₂ than faster-spread crust of similar age^{2,3} (Fig. 3 and Extended Data Table 1). The CO₂ content of the U1557 breccia is therefore 2 to 40 times that of previously sampled upper ocean crust.

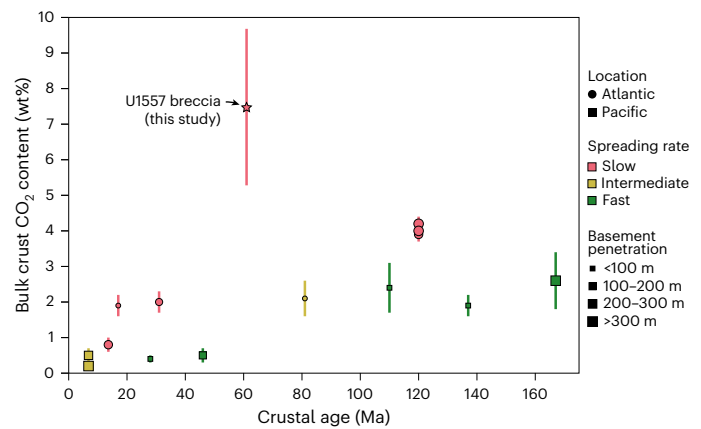


Fig. 3 | Bulk carbon dioxide contents of upper ocean crustal sections versus crustal age. The mean CO₂ content of the U1557 breccia cores (star), weighted by core interval lengths to normalize to core recovery, is compared to bulk CO₂ contents of previously drilled sections of intact, in situ, upper ocean crust^{2,3}. Symbol colours indicate spreading rate as defined in ref. 52, with circles and squares representing drill sites located in the Atlantic and Pacific Oceans, respectively. Symbol size indicates basement penetration achieved at each site. Ridge flank carbon uptake is assumed to predominantly occur within the upper 300 m of the crust², with greater penetration giving more confidence in the estimated carbon content of this sink. Error bars for the U1557 data are the standard deviation of the mean CO₂ content of the cores, weighted by their drilled interval lengths ($n = 17$; Methods) and reflect the lithological heterogeneity of the talus breccia relative to typical upper crustal basalts. For other sites, data for each drillhole are reported with error bars representing reported propagated analytical errors³. Data and their sources are given in Extended Data Table 1.

A talus breccia-hosted global carbon cycle sink

The ridge flank hydrothermal carbon sink has previously been quantified from analyses of ~7 to 170-Ma upper ocean crust^{2,3}. We consider the U1557 breccia-hosted carbonate to be a distinct additional ridge flank hydrothermal carbon sink because such talus breccias accumulate on top of the volcanic crust from which the global upper crustal carbon reservoir has previously been estimated, with the carbon they host therefore not included in those estimates. To represent an important reservoir in the long-term geological carbon cycle, talus breccia-hosted carbonate must occur elsewhere on the ridge flanks in substantial volumes. Given a talus breccia CO₂ content 2 to 40 times that of upper crustal lavas, breccia deposits need only be 2.5 to 50% the thickness of the CO₂-uptake zone in the underlying crust to host the same carbon sink. The ridge flank carbon sink has previously been estimated assuming uptake occurs predominantly within the upper 300 m of crust^{2,3}, although only four of the studied drill holes penetrate to that depth (Fig. 3).

Ocean crust is currently being produced at a rate of 3.4 km² per year³³, resulting in an estimated magmatic outgassing of $0.47\text{--}2.09 \times 10^{12}$ moles CO₂ (ref. 1)—equivalent to $14\text{--}61 \times 10^{10}$ moles CO₂ per km² of new crust. The extent to which CaCO₃ precipitation in talus breccias that subsequently accumulate on that crust buffers this release, globally, depends on both the bulk CO₂ content and average thickness of the breccia, per km² of crust (Fig. 4a).

At slow-spreading rates, talus breccia piles are common along the normal fault scarps of the modern axial valley walls, evolving from small talus fans to wedge-shaped deposits that cover most of the lower fault slope over ~1 Myr as the faults grow^{34,35} (Extended Data Fig. 1). The planar upper surface of mature deposits is controlled by the angle of repose of the talus clasts (typically 25–40° (ref. 24)). These breccia deposits are rafted across the ocean basin floor with the axial faults as spreading continues at the ridge, over which time their geometry may be modified.

To assess the average thickness of breccia potentially generated by axial valley faults we modelled their breccia deposits as ridge-parallel triangular prisms with their upper and lower surfaces defined by the angle of repose (R) and fault dip (F), respectively (Extended Data Fig. 1). The average thickness of breccia per km² of ocean crust (T_B), is given by:

$$T_B = \frac{x^2}{200} \dot{\epsilon} \left[\frac{\tan F}{\tan R} - 1 \right] \bar{t} \quad (1)$$

where x is the proportion of the fault scarp covered by talus, \bar{t} is the average fault throw and $\dot{\epsilon}$ is the tectonic strain (%) across the plate boundary (Methods provide derivation).

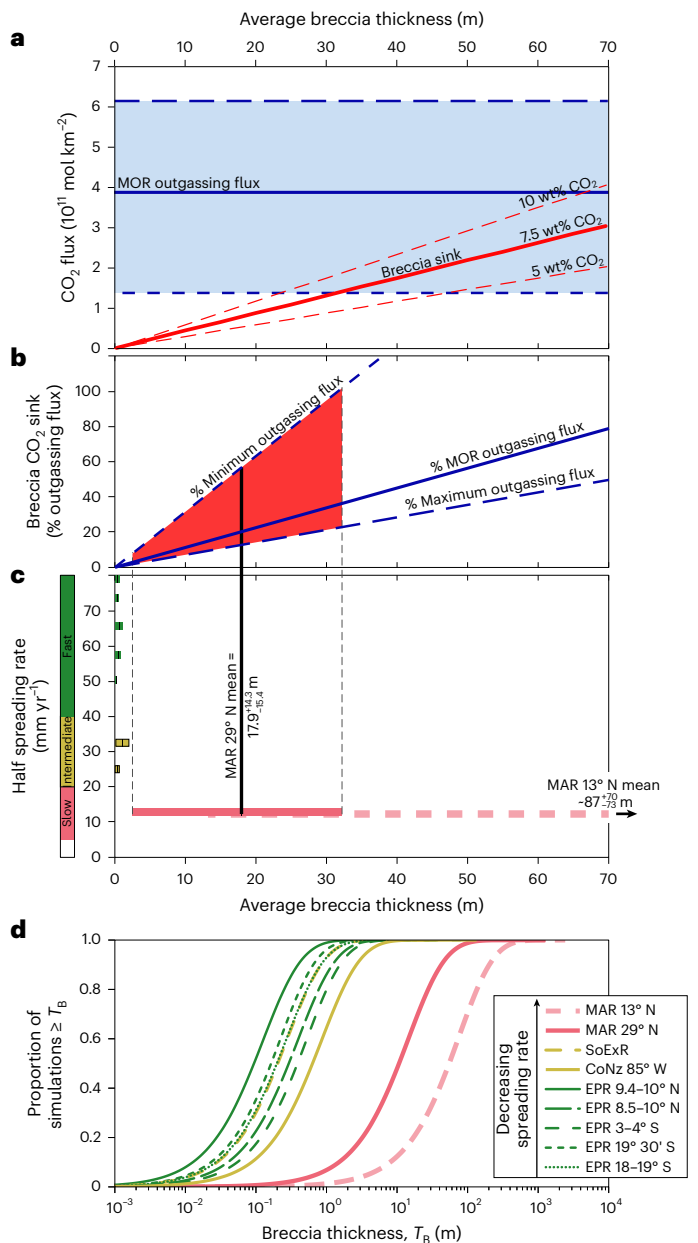
Using detailed observations of normal fault and talus deposit geometries and tectonic strain along the modern Mid-Atlantic Ridge at 29° N (refs. 21,35) we estimate a mean talus breccia thickness of 18⁺¹⁴₋₁₅ m (1 σ equivalent) will accumulate on crust produced at this ridge segment, which has crustal architecture typical of slow-spread crust without low-angle oceanic detachment faults. The uncertainty in this estimate was robustly constrained using parametric bootstrapping (Methods and Extended Data Fig. 2). Assuming a CO₂ content of 7.5 wt% and bulk density of 2,570 kg m⁻³, such an average talus breccia thickness would host 7.8^{+6.3}_{-6.7} × 10¹⁰ moles CO₂ km⁻². This is equivalent to 20⁺¹⁶₋₁₇% of the best estimate of the CO₂ released during formation of the underlying crust, although given the similar uncertainty in the MOR outgassing flux it could be equivalent to as much as 102% of the CO₂ released (Fig. 4b).

Because average fault throws and tectonic strain vary substantially along the global MOR system, the average talus breccia thickness per km² ocean crust is expected to vary substantially, too. Axial grabens are common on intermediate-spreading ridges, and faulting occurs at all spreading rates—albeit with smaller throws and lower tectonic strain at faster spreading rates³⁵. Although the global average talus breccia thickness remains unknown, talus abundance is predicted to increase nonlinearly with decreasing spreading rate (Fig. 4d and Extended Data Figs. 3 and 4). Crucially, the global talus-hosted CO₂ sink should therefore have varied in response to global changes in spreading rate³⁶, in contrast to the CO₂-outgassing flux, which is independent of spreading rate¹.

Fig. 4 | Comparison of MOR CO₂-outgassing and talus breccia CO₂ uptake fluxes. **a**, Comparison of the potential ocean crustal breccia CO₂ sink with the estimated MOR outgassing flux¹ (solid blue line) per km² of ocean crust. The uncertainty in global MOR outgassing flux¹ is indicated by the blue shaded region, with the maximum and minimum estimates indicated by long- and short-dashed blue lines, respectively. The magnitude of the talus breccia CO₂ sink (red lines) depends on both its average thickness and CO₂ content (7.5 wt% at Site U1557; solid red line). **b**, The CO₂ sink hosted by talus breccia with 7.5 wt% CO₂, expressed as a proportion of the estimated MOR CO₂-outgassing flux to illustrate its relative magnitude, as a function of average breccia thicknesses. The solid, long- and short-dashed blue lines indicate the proportion of the mean, maximum and minimum estimates of the outgassing flux, respectively. **c**, Estimates of the average breccia thickness along segments of the slow-spreading Mid-Atlantic Ridge (MAR) (red), intermediate-spreading Southern Explorer (SoExR) and Cocos-Nazca (CoNz) Ridges (yellow) and fast-spreading East Pacific Rise (EPR) (green), calculated from observations of fault and talus geometries and tectonic strain using parametric bootstrapping (Methods and Supplementary Table 4). Coloured bars indicate uncertainty in the estimated mean thickness (1 σ equivalent). **d**, Distributions of simulated breccia thicknesses (T_B) used to calculate the mean thicknesses displayed in **c**. Breccia thickness in the MAR 13° N area (dashed light red bar/line in **c** and **d**, respectively) is only estimated on crust not affected by low-angle detachment faulting (that is, on the ridge flank opposite the oceanic core complexes) and is therefore interpreted with caution here (Methods). The red shaded region in **b** indicates the uncertainty in the extent to which talus breccia of the average thickness estimated for the MAR at 29° N (assuming a CO₂ content of 7.5 wt%) could accommodate the CO₂ outgassed during formation of the underlying crust, given the uncertainties in both the MOR CO₂-outgassing flux and the estimated average breccia thickness.

Prolonged CO₂ uptake in talus breccias on slow-spread crust

CaCO₃ precipitated within ocean crust records the Sr isotopic composition and temperature of the fluids it forms from³⁷. Strontium exchange during fluid–rock reaction lowers the ⁸⁷Sr/⁸⁶Sr ratios of ridge flank basement fluids from their initial seawater compositions towards that of basalt (−0.703³⁸), with most fluid heated as it reacts with, and cools, the crust^{37,39}. The ⁸⁷Sr/⁸⁶Sr ratio of seawater since 61 Ma is well established from marine biogenic carbonate sediments⁴⁰ and has ranged between a minimum of 0.707715 ± 0.000010 (53.5 million years ago) and the modern ratio of 0.70918 (Fig. 5a). Whether the U1557 carbonates record seawater Sr isotopic compositions or contain a basaltic Sr component depends on when they precipitated. Approximately half of the sparry carbonate cements have Sr isotopic compositions between 0.707865 and 0.708305 (Fig. 5c and Supplementary Table 3), falling within the blue shaded region of Fig. 5a, consistent with their formation either from seawater between 34 and 23 Ma (that is, 27 to 38 Myr after the crust formed) or more recently if they precipitated from a fluid containing some basalt-derived Sr. Most of these carbonates formed between 630 and 650 metres below seafloor (mbsf) in an interval overlying a



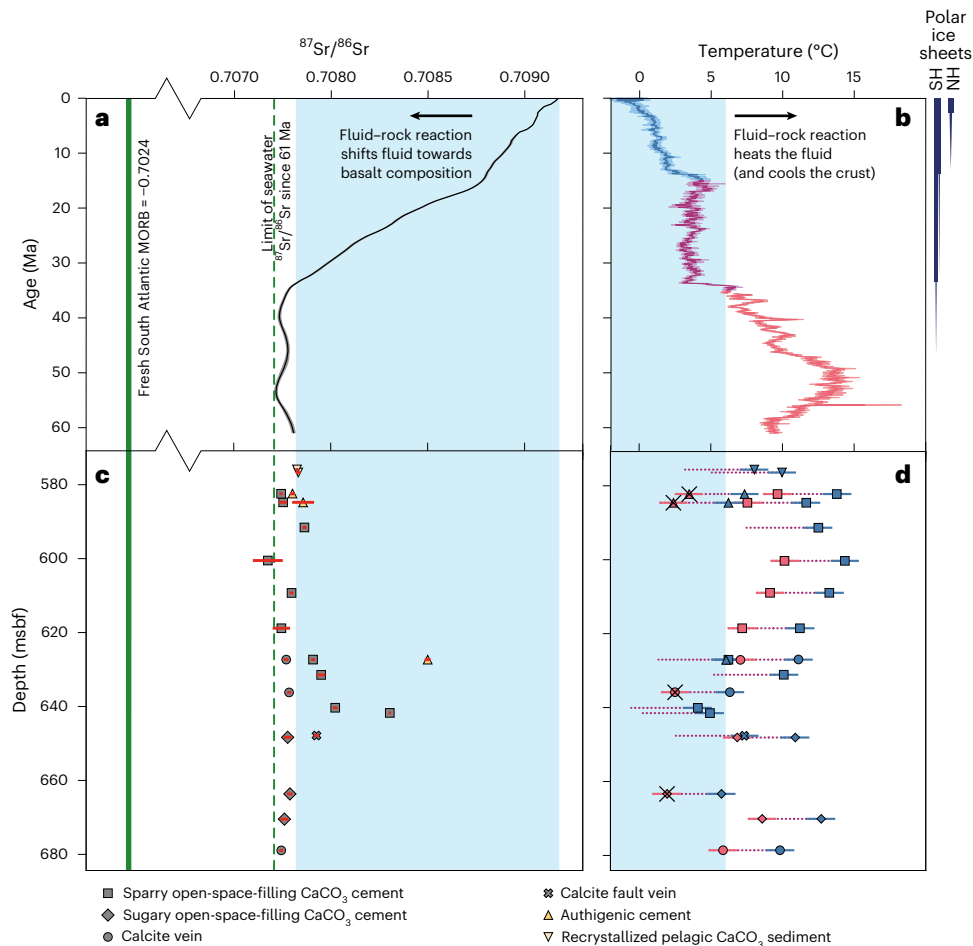


Fig. 5 | Comparison of fluid strontium isotopic composition and temperatures recorded by U1557 carbonates with seawater records since the crust formed.

Symbol shapes indicate carbonate type. **a**, Seawater $^{87}\text{Sr}/^{86}\text{Sr}$ ⁴⁰; fluid–rock reactions shift fluid compositions towards fresh mid-ocean ridge basalt (MORB; solid green line⁵³). **b**, Bottom-water temperature (Supplementary Methods). Polar ice sheet distributions to right, following ref. 54; SH, southern hemisphere; NH, northern hemisphere. **a–d**, Blue shading shows bottom seawater $^{87}\text{Sr}/^{86}\text{Sr}$ (**a,c**) and temperature ranges (**b,d**) since 34 Ma. **c**, Carbonate $^{87}\text{Sr}/^{86}\text{Sr}$; data are presented as mean values and red error bars indicate analytical uncertainty ($\pm 2\text{SE}$; Supplementary Table 3). **d**, Precipitation temperatures calculated from carbonate $\delta^{18}\text{O}$ following ref. 55, assuming basement fluids have $\delta^{18}\text{O}$ of contemporaneous seawater^{42,43}. As U1557 carbonates could have precipitated

at any time since 61 Ma, endmember temperatures are calculated for ice-free oceans ($\delta^{18}\text{O}_{\text{seawater}} = -1\text{‰}$; red symbols) and oceans with established ice sheets ($\delta^{18}\text{O}_{\text{seawater}} = 0\text{‰}$; blue symbols), with intermediate values (purple dashes) when ice sheets wax/wane (corresponding to red, blue and purple intervals in **b**, respectively). Data are presented as calculated temperatures with conservative error bars of $\pm 1\text{ °C}$ reflecting the potential uncertainty due to the choice of thermometer (Supplementary Methods for discussion). Where $^{87}\text{Sr}/^{86}\text{Sr}$ compositions require formation since 34 Ma (blue shaded region of **c**) ice-free temperatures are not shown. Precipitation temperatures colder than the overlying oceans are not possible (‘ice-free’ temperatures within blue shaded region of **d**), as indicated by crosses.

carbonate-cemented fault zone that may have promoted prolonged fluid flow through the breccia deposit (Fig. 2c). However, the remaining vein and cement carbonates have $^{87}\text{Sr}/^{86}\text{Sr}$ ratios lower than 34 Ma seawater (Fig. 5c) and could have precipitated as early as 0–5 Myr after crustal formation, given the fluctuations in seawater composition between 61 and 34 Ma (Fig. 5a).

Precipitation temperatures determined from carbonate oxygen isotopic compositions ($\delta^{18}\text{O}$; Supplementary Table 3) provide additional constraints on when the carbonates precipitated and the nature of the fluid they formed from. Calculated temperatures depend on the fluid $\delta^{18}\text{O}$, which is assumed to remain unmodified during low-temperature reactions with basalt^{37,39,41}. Between 61 and 35 Ma, the oceans were ice free, with seawater $\delta^{18}\text{O}$ of -1‰ (refs. 42,43). Using this ice-free fluid composition yields temperatures colder than 61–35 Ma seawater for many of our samples (Fig. 5b,d). However, the upper crust, and hence fluids flowing through it, cannot be cooler than bottom seawater. This suggests these carbonates formed more recently when the oceans were cooler (Fig. 5b) from fluids warmer than contemporaneous seawater, with a basaltic Sr component. The minimum duration of

carbon uptake is recorded by an authigenic cement overgrowing and hence post-dating void-filling carbonate. It has a more radiogenic Sr isotopic composition of 0.7085, the composition of 19-Ma seawater, requiring precipitation at least 42 Myr after the crust formed (Fig. 5a,c).

Collectively, the carbonate cements, veins and matrix from the U1557 talus breccia record circulation of $<15\text{ °C}$ seawater and/or seawater-derived fluids modified by reaction with basalt through the breccia for at least 42 million years on the southern Mid-Atlantic Ridge flank. This is substantially longer than observations from well-sedimented ridge flanks with more subdued basement topography⁴⁴. This suggests that spreading rate not only influences the extent of CO_2 uptake by ocean crust but also the duration of basement carbonate precipitation.

Spreading rate and crustal age controls on carbon uptake

The discovery of a talus breccia-hosted carbon reservoir on the western flank of the slow-spreading southern Mid-Atlantic Ridge highlights the importance of upper crustal architecture when modelling the role of

mid-ocean spreading in the long-term geological carbon cycle. The high primary porosity and large surface area of the U1557 basaltic talus breccia allow it to act as a geological sponge for the precipitation of dissolved seawater carbon in carbonate minerals. Other types of porous basaltic breccia form along the ridge axes through both magmatic processes and the collapse of volcanic cones⁴⁵ or through mass wasting along oceanic fracture zones⁴⁶ or on the flanks of seamounts. We would expect CaCO₃ to precipitate in these breccias as well, as their host crust ages. U1557 cored the base of a faulted basin interpreted to be typical of axial valley normal faulting, indicating that CaCO₃-cemented talus breccias are probably a global phenomenon on slow- to intermediate-spreading-rate crust. Consequently, past variations in the global lengths of slow-, intermediate- and fast-spreading ridges³⁶ probably caused shifts in the relative magnitude of the carbon fluxes during mid-ocean ridge CO₂ outgassing and carbonate formation on the ageing ridge flanks. The tectonic component of plate divergence at slow-spreading ridges that generates talus breccias also results in rough basement topography that remains incompletely covered by sediments for tens of millions of years on the ridge flanks, promoting prolonged fluid flow and carbonate precipitation in the upper crust. As spreading rate also influences the duration of CO₂ uptake, models of the past contributions of ridge flanks to the long-term carbon cycle need to also allow for variations in the age-area distribution of the ocean crust³⁶ as a function of spreading rate.

Online content

Any methods, additional references, Nature Portfolio reporting summaries, source data, extended data, supplementary information, acknowledgements, peer review information; details of author contributions and competing interests; and statements of data and code availability are available at <https://doi.org/10.1038/s41561-025-01839-5>.

References

- Le Voyer, M. et al. Carbon fluxes and primary magma CO₂ contents along the global mid-ocean ridge system. *Geochem. Geophys. Geosyst.* **20**, 1219–1675 (2019).
- Alt, J. C. & Teagle, D. A. H. The uptake of carbon during alteration of ocean crust. *Geochim. Cosmochim. Acta* **63**, 1527–1535 (1999).
- Gillis, K. M. & Coogan, L. A. Secular variation in carbon uptake into the ocean crust. *Earth Planet. Sci. Lett.* **302**, 385–392 (2011).
- Kelemen, P. B. & Manning, C. E. Reevaluating carbon fluxes in subduction zones, what goes down, mostly comes up. *Proc. Natl Acad. Sci. USA* **112**, E3997–E4006 (2015).
- Berner, R. A., Lasaga, A. C. & Garrels, R. M. The carbonate-silicate geochemical cycle and its effect on atmospheric carbon dioxide over the last 100 million years. *Am. J. Sci.* **283**, 641–683 (1983).
- Coogan, L. A. & Dosso, S. Alteration of ocean crust provides a strong temperature dependent feedback on the geological carbon cycle and is a primary driver of the Sr-isotopic composition of seawater. *Earth Planet. Sci. Lett.* **415**, 38–46 (2015).
- Coogan, L. A. & Gillis, K. M. Low-temperature alteration of the seafloor: impacts on ocean chemistry. *Annu. Rev. Earth Planet. Sci.* **46**, 21–45 (2018).
- Müller, R. D. & Dutkiewicz, A. Oceanic crustal carbon cycle drives 26-million-year atmospheric carbon dioxide periodicities. *Sci. Adv.* **4**, eaaq0500 (2018).
- Staudigel, H., Hart, S. R., Schmincke, H. U. & Smith, B. M. Cretaceous ocean crust at DSDP sites 417 and 418: carbon uptake from weathering versus loss by magmatic outgassing. *Geochim. Cosmochim. Acta* **53**, 3091–3094 (1989).
- Mottl, M. J. in *Energy and Mass Transfer in Marine Hydrothermal Systems* (eds Halbeck, P. E. et al.) 271–286 (Dahlem Univ. Press, 2003).
- Lister, C. R. B. On the thermal balance of a mid-ocean ridge. *Geophys. J. R. Astron. Soc.* **26**, 515–535 (1972).
- Stein, C. A. & Stein, S. Constraints on hydrothermal heat-flux through the oceanic lithosphere from global heat-flow. *J. Geophys. Res.* **99**, 3081–3095 (1994).
- Von Herzen, R. P. & Uyeda, S. Heat flow through the eastern Pacific floor. *J. Geophys. Res.* **68**, 4219–4250 (1963).
- Fisher, A. T. & Harris, R. N. Using seafloor heat flow as a tracer to map subsurface fluid flow in the ocean crust. *Geofluids* **10**, 142–160 (2010).
- Fisher, A. T. & Becker, K. Channelized fluid flow in oceanic crust reconciles heat-flow and permeability data. *Nature* **403**, 71–74 (2000).
- Evans, A. D. et al. Ocean crustal veins record dynamic interplay between plate-cooling-induced cracking and ocean chemistry. *Earth Planet. Sci. Lett.* **650**, 119116 (2025).
- Coggon, R. M. et al. *Proc. of the International Ocean Discovery Program Vol. 390/393* (International Ocean Discovery Program, 2024).
- Teagle, D. A. H., Ildefonse, B., Blum, P. & the Expedition 335 Scientists. *Proceedings of the Integrated Ocean Drilling Program vol. 335* (Integrated Ocean Drilling Program Management International Inc., 2012).
- MacDonald, K. C. Mid-ocean ridges: fine scale tectonic, volcanic and hydrothermal processes within the plate boundary zone. *Ann. Rev. Earth Planet. Sci.* **10**, 155–190 (1982).
- Thibaud, R., Gente, P. & Maia, M. A systematic analysis of the Mid-Atlantic Ridge morphology and gravity between 15°N and 40°N: constraints of the thermal structure. *J. Geophys. Res. Solid Earth* **103**, 24223–24243 (1998).
- Escartin, J. et al. Quantifying tectonic strain and magmatic accretion at slow spreading ridge segment, Mid-Atlantic Ridge, 29°N. *J. Geophys. Res.* **104**, 10421–10437 (1999).
- Olive, J. A. & Dublanchet, P. Controls on the magmatic fraction of extension at mid-ocean ridges. *Earth Planet. Sci. Lett.* **549**, 116541 (2020).
- Allerton, S., Murton, B. J., Searle, R. C. & Jones, M. Extensional faulting and segmentation of the Mid-Atlantic Ridge north of the Kane Fracture Zone (24°00'N to 24°40'N). *Mar. Geophys. Res.* **17**, 37–61 (1995).
- Cannat, M., Mangeney, A., Ondréas, H., Fouquet, Y. & Normand, A. High-resolution bathymetry reveals contrasting landslide activity shaping the walls of the Mid-Atlantic Ridge axial valley. *Geochem. Geophys. Geosyst.* **14**, 996–1011 (2013).
- Estep, J., Reece, R., Christeson, G. L., Kardell, D. A. & Carlson, R. L. 70 million years of seafloor spreading and magmatism in the South Atlantic. *Earth Planet. Sci. Lett.* **574**, 117173 (2021).
- Kardell, D. A., Christeson, G. L., Estep, J. D., Reece, R. S. & Carlson, R. L. Long-lasting evolution of layer 2A in the western South Atlantic: evidence for low-temperature hydrothermal circulation in old oceanic crust. *J. Geophys. Res.: Solid Earth* **124**, 2252–2273 (2019).
- Christeson, G. L. et al. South Atlantic Transect: variations in oceanic crustal structure at 31°S. *Geochem. Geophys. Geosyst.* **21**, e2020GC009017 (2020).
- Estep, J., Reece, R., Kardell, D. A., Christeson, G. L. & Carlson, R. L. Seismic Layer 2A: evolution and thickness from 0- to 70-Ma crust in the slow-intermediate spreading South Atlantic. *J. Geophys. Res.: Solid Earth* **124**, 7633–7651 (2019).
- Carbotte, S. & MacDonald, K. C. Comparison of seafloor tectonic fabric at intermediate, fast, and super fast spreading ridges: influence of spreading rate, plate motions, and ridge segmentation on fault patterns. *J. Geophys. Res.: Solid Earth* **99**, 13609–13631 (1994).
- Ito, G. & Behn, M. D. Magmatic and tectonic extension at mid-ocean ridges: 2. origin of axial morphology. *Geochem. Geophys. Geosyst.* **9**, Q09O12 (2008).
- Alt, J. C. in *Hydrogeology of the Oceanic Lithosphere* (eds Davis, E. & Elderfield, H.) 456–488 (Cambridge Univ. Press, 2004).
- Gradstein, F. M., Ogg, J. G., Schmitz, M. D. & Ogg, G. M. *Geologic Time Scale 2020* (Elsevier, 2020).

33. Rowley, D. B. Rate of plate creation and destruction: 180 Ma to present. *Geol. Soc. Am. Bull.* **114**, 927–933 (2002).
34. Allerton, S., Searle, R. C. & Murton, B. J. Bathymetric segmentation and faulting on the Mid-Atlantic Ridge, 24°00'N to 24°40'N. *Geol. Soc. London Spec. Publ.* **118**, 49–60 (1996).
35. Searle, R. in *Mid-Ocean Ridges* Ch. 7, 163–199 (Cambridge Univ. Press, 2013).
36. Müller, R. D., Sdrolias, M., Gaina, C. & Roest, W. R. Age, spreading rates, and spreading asymmetry of the world's ocean crust. *Geochem. Geophys. Geosyst.* **9**, Q04006 (2008).
37. Coggon, R. M., Teagle, D. A. H., Cooper, M. J. & Vanko, D. A. Linking basement carbonate vein compositions to porewater geochemistry across the eastern flank of the Juan de Fuca Ridge, ODP Leg 168. *Earth Planet. Sci. Lett.* **219**, 111–128 (2004).
38. Elderfield, H., Wheat, C. G., Mottl, M. J., Monnin, C. & Spiro, B. Fluid and geochemical transport through oceanic crust: a transect across the eastern flank of the Juan de Fuca Ridge. *Earth Planet. Sci. Lett.* **172**, 151–165 (1999).
39. Coggon, R. M., Teagle, D. A. H., Smith-Duque, C. E., Alt, J. C. & Cooper, M. J. Reconstructing past seawater Mg/Ca and Sr/Ca from mid-ocean ridge flank calcium carbonate veins. *Science* **327**, 1114–1117 (2010).
40. McArthur, J. M., Howarth, R. J. & Bailey, T. R. Strontium isotope stratigraphy: LOWESS version 3. best-fit line to the marine Sr-isotope curve for 0 to 509 Ma and accompanying look-up table for deriving numerical age. *J. Geol.* **109**, 155–169 (2001).
41. Coggon, R. M. & Teagle, D. A. H. Hydrothermal calcium-carbonate veins reveal past ocean chemistry. *Trends Anal. Chem.* **30**, 1252–1268 (2011).
42. Meckler, A. N. et al. Cenozoic evolution of deep ocean temperature from clumped isotope thermometry. *Science* **377**, 86–90 (2022).
43. Cramer, B. S., Miller, K. G., Barrett, P. J. & Wright, J. D. Late Cretaceous-Neogene trends in deep ocean temperature and continental ice volume: reconciling records of benthic foraminiferal geochemistry ($\delta^{18}\text{O}$ and Mg/Ca) with sea level history. *J. Geophys. Res.* *Oceans* **116**, C12023 (2011).
44. Coogan, L. A., Parrish, R. R. & Roberts, N. M. W. Early hydrothermal carbon uptake by the upper oceanic crust: insight from in situ U-Pb dating. *Geology* **44**, 147–150 (2016).
45. Yeo, I., Searle, R. C., Achenbach, K. L., Le Bas, T. P. & Murton, B. J. Eruptive hummocks: building blocks of the upper ocean crust. *Geology* **40**, 91–94 (2012).
46. Bonatti, E. & Hartman, K. in *Initial Reports of the Deep Sea Drilling Project* Vol. 39 (eds Supko, P. R. et al.) 507–511 (US Government Printing Office, 1977).
47. Ryan, W. B. F. et al. Global multi-resolution topography synthesis. *Geochem. Geophys. Geosyst.* **10**, Q03014 (2009).
48. Seton, M. et al. A global data set of present-day oceanic crustal age and seafloor spreading parameters. *Geochem. Geophys. Geosyst.* **21**, e2020GC009214 (2020).
49. Reece, R. & Estep, J. Processed MCS (PSTM) data from the Mid-Atlantic Ridge (MAR) to the Rio Grande Rise, South Atlantic Ocean, acquired by the R/V Marcus G. Langseth in 2016 (MGL1601). *MGDS* <https://doi.org/10.1594/IEDA/500255> (2019).
50. Fisher, A. T. et al. Hydrothermal recharge and discharge across 50 km guided by seamounts on a young ridge flank. *Nature* **421**, 618–621 (2003).
51. Wheat, C. G. & Fisher, A. T. Massive, low-temperature hydrothermal flow from a basaltic outcrop on 23 Ma seafloor of the Cocos Plate: chemical constraints and implications. *Geochem. Geophys. Geosyst.* **9**, Q12014 (2008).
52. Christeson, G. L., Goff, J. A. & Reece, R. S. Synthesis of oceanic crustal structure from two-dimensional seismic profiles. *Rev. Geophys.* **57**, 504–529 (2019).
53. Hoernle, K. et al. On- and off-axis chemical heterogeneities along the South Atlantic Mid-Ocean-Ridge (5–11°S): shallow or deep recycling of ocean crust and/or intraplate volcanism?. *Earth Planet. Sci. Lett.* **306**, 86–97 (2011).
54. Westerhold, T. et al. An astronomically dated record of Earth's climate and its predictability over the last 66 million years. *Science* **369**, 1383–1387 (2020).
55. Friedman, I. & O'Neil, J. R. in *Data of Geochemistry United States Geological Survey Professional Paper 440-KK* (ed. Fleischer, M.) 1–12 (USGS, 1977).

Publisher's note Springer Nature remains neutral with regard to jurisdictional claims in published maps and institutional affiliations.

Open Access This article is licensed under a Creative Commons Attribution 4.0 International License, which permits use, sharing, adaptation, distribution and reproduction in any medium or format, as long as you give appropriate credit to the original author(s) and the source, provide a link to the Creative Commons licence, and indicate if changes were made. The images or other third party material in this article are included in the article's Creative Commons licence, unless indicated otherwise in a credit line to the material. If material is not included in the article's Creative Commons licence and your intended use is not permitted by statutory regulation or exceeds the permitted use, you will need to obtain permission directly from the copyright holder. To view a copy of this licence, visit <http://creativecommons.org/licenses/by/4.0/>.

© The Author(s) 2025

¹School of Ocean and Earth Science, National Oceanography Centre Southampton, University of Southampton, Southampton, UK. ²School of Life Sciences, Keele University, Newcastle-under-Lyme, UK. ³University of Texas Institute for Geophysics, University of Texas at Austin, Austin, TX, USA. ⁴Department of Geology, Kansas State University, Manhattan, KS, USA. ⁵Institute of Geosciences, Christian-Albrechts-University of Kiel, Kiel, Germany. ⁶Section of Geophysics, Alfred Wegener Institute, Helmholtz Centre for Polar and Marine Research, Bremerhaven, Germany. ⁷School of Earth and Sustainability, Northern Arizona University, Flagstaff, AZ, USA. ⁸Marine Geology and Geophysics, National Science Foundation, Alexandria, VA, USA. ⁹School of Geography, Earth and Environmental Sciences, University of Plymouth, Plymouth, UK. ¹⁰UCD School of Earth Sciences, University College Dublin, Dublin, Ireland. ¹¹Department of Oceanography, Texas A&M University, College Station, TX, USA. ¹²Department of Geology and Geophysics, Texas A&M University, College Station, TX, USA. ¹³International Ocean Discovery Program, Texas A&M University, College Station, TX, USA. ¹⁴Present address: Marine Geology and Geophysics, National Science Foundation, Alexandria, VA, USA. ¹⁵These authors contributed equally: Rosalind M. Coggon, Elliot J. Carter, Lewis J. C. Grant, Aled D. Evans. *A list of authors and their affiliations appears at the end of the paper. ✉e-mail: R.M.Coggon@soton.ac.uk

The South Atlantic Transect IODP Expedition 390 & 393 Scientists

Rosalind M. Coggon^{1,15}, Elliot J. Carter^{2,15}, Lewis J. C. Grant^{1,15}, Aled D. Evans^{1,15}, Christopher M. Lowery³, Damon A. H. Teagle¹, Pamela D. Kempton⁴, Claire M. Routledge⁵, Elmar Albers⁶, Justin Estep⁷, Gail L. Christeson⁸, Michelle Harris⁹, Thomas M. Belgrano¹⁰, Jason B. Sylvan¹¹, Julia S. Reece¹², Emily R. Estes^{13,14} & Trevor Williams¹³

A full list of members and their affiliations appears in the Supplementary Information

Methods

The magnitude of the carbon sink that talus breccias accumulated on top of the ocean crust constitute depends on the breccia's bulk CO₂ content and its average thickness, per km² of crust.

Quantifying the carbon content of the U1557 talus breccia

To quantify the talus breccia-hosted carbon sink it is necessary to know the carbon content of the carbonate-bearing components in the breccia. On the basis of examination in hand specimen and thin sections and the results of shipboard X-ray diffraction analyses¹⁷, sparry and sugary carbonate cements constitute pure or almost pure calcite, which contains 44 wt% CO₂. The mean CO₂ content of the recrystallized pelagic carbonate sediment matrix present in the uppermost -20 m of the breccia (43.3 wt%, $n = 5$; Supplementary Table 2) indicates that it is near-pure carbonate, consistent with the composition of the overlying sedimentary sequence¹⁷. In contrast, the microcrystalline authigenic cement from below -20 m sub-basement constitutes a mixture of phillipsite zeolite and carbonate material. This material was estimated to constitute approximately 50 vol% carbonate based on petrographic observations¹⁷. Three samples of the authigenic material have CO₂ contents ranging from 17 to 28 wt% (Supplementary Table 2), with a mean value of 26 wt%, consistent with the petrographic observations. Carbonate also replaces primary minerals and fills interstitial space in the basalt clasts, which consequently have CO₂ contents ranging from 0.1 to 5.1 wt% with a mean of 1.0 wt% ($n = 46$; Supplementary Table 2).

The CO₂ content of each core, [CO₂]_{*x*} (Supplementary Table 1), was calculated from the volume proportions of the CO₂-bearing components in each core (V_{i-x}) following:

$$[\text{CO}_2]_x = \sum_i [\text{CO}_2]_{i-x} = \sum_i V_{i-x} \left(\frac{\rho_i}{\rho_x} \right) [\text{CO}_2]_i \quad (2)$$

where [CO₂]_{*i-x*} is the contribution to [CO₂]_{*x*} from component *i*, ρ_x is the bulk density of core *x*, and ρ_i and [CO₂]_{*i*} are the density and CO₂ content (wt%; Supplementary Table 1) of component *i*, respectively. The bulk density of each core was calculated from the mean bulk densities for Site U1557 breccia clasts, sediment matrix and authigenic cement determined during shipboard physical properties measurements (2,610; 2,400 and 2,300 kg m⁻³, respectively¹⁷), assuming the mean density of non-carbonate secondary minerals is that of breccia clasts and the density of calcite cement is 2,710 kg m⁻³:

$$\rho_x = \sum_i V_{i-x} \rho_i \quad (3)$$

The average CO₂ content of the breccia deposit was calculated from core CO₂ contents, weighted by core interval lengths (L_x) to normalize for variable core recovery:

$$[\text{CO}_2]_{\text{Breccia}} = \frac{\sum_x L_x \rho_x [\text{CO}_2]_x}{\sum_x L_x \rho_x} \quad (4)$$

where $\sum_x L_x \rho_x$ is the bulk density of the breccia (2,570 kg m⁻³).

Thickness of talus breccia accumulated on ocean crust

To assess the potential global volume of talus breccia on slow-spread crust, we model talus breccia deposits as ridge-parallel triangular prisms with their upper and lower surfaces defined by the angle of repose (R) and fault dip (F), respectively (Extended Data Fig. 1). The triangular cross-sectional area of the breccia wedge (A) is given by:

$$A = \frac{1}{2} (xt) (d + xh) - \frac{1}{2} (xt) (xh) = \frac{1}{2} xtd \quad (5)$$

where t and h are the fault's throw and heave, respectively; x is the proportion of the fault scarp covered by talus, such that xt is the height

of the breccia pile and xh is the horizontal width of fault covered by breccia; and d is the distance the talus pile extends from the fault (Extended Data Fig. 1). From trigonometry:

$$\tan R = \frac{xt}{d + xh} \quad (6)$$

and

$$\tan F = \frac{t}{h} \quad (7)$$

Combining equations (6) and (7) gives the expression:

$$d = xt \left(\frac{1 - \frac{\tan R}{\tan F}}{\tan R} \right) \quad (8)$$

Consequently, the cross-sectional area of the breccia wedge can be expressed in terms of x , t , R and F :

$$A = \frac{x^2 t^2}{2 \tan R} \left[1 - \frac{\tan R}{\tan F} \right] \quad (9)$$

The volume of breccia, V_B , on an area of seafloor of width W perpendicular to the ridge axis and length L parallel to the ridge is the product of the average volume of breccia wedges in the area ($\bar{A}L$, where \bar{A} is the average cross-sectional area of the wedges) and the number of breccia wedges across that crustal width (W/S , where S is the average fault spacing; Extended Data Fig. 1d):

$$V_B = (\bar{A}L) \left(\frac{W}{S} \right) = \frac{x^2 (\bar{t})^2}{2 \tan R} \left[1 - \frac{\tan R}{\tan F} \right] L \frac{W}{S} \quad (10)$$

where \bar{t} is the average fault throw. The average thickness of breccia per unit area of ocean crust, T_B (the thickness if the wedge-shaped deposits were spread out to form a layer of uniform thickness, evenly across the entire area), is therefore given by:

$$T_B = \frac{V_B}{WL} = \frac{x^2 (\bar{t})^2}{2S \tan R} \left[1 - \frac{\tan R}{\tan F} \right] \quad (11)$$

The proportion of plate divergence accommodated by faulting (% strain; ε) increases with decreasing spreading rate³⁵. The strain across the plate boundary is a function of fault size and spacing:

$$\varepsilon = 100 \left(\frac{h}{S} \right) \quad (12)$$

Combining equations (7) and (12), the fault spacing can be expressed as:

$$S = 100 \left(\frac{\bar{t}}{\varepsilon \tan F} \right) \quad (13)$$

and combining equations (11) and (13), the average breccia thickness per unit area of ocean crust is given by:

$$\begin{aligned} T_B &= \frac{x^2}{200} \varepsilon \left[\frac{\tan F}{\tan R} \right] \left[1 - \frac{\tan R}{\tan F} \right] \bar{t} \\ &= \frac{x^2}{200} \varepsilon \left[\frac{\tan F}{\tan R} - 1 \right] \bar{t} \end{aligned} \quad (14)$$

The average breccia thickness is therefore proportional to both fault throw and strain (Extended Data Fig. 3). Normal faulting occurs across the full spectrum of mid-ocean spreading rates. Along ridges spreading at full rates below 60–70 mm yr⁻¹ sub-axial magma chambers

are episodic, and the melt supply is <90% of that required by plate separation³⁵. Tectonic strain accommodates the remainder of the plate separation, with the average fault throw orders of magnitude greater than at fast-spreading ridges (Supplementary Table 4). As both average fault throw and strain increase with decreasing spreading rate, the average talus breccia thickness is expected to be greatest on slow-spread crust. However, breccia should accumulate to some extent on crust produced at all spreading rates if there is a component of tectonic strain across the plate boundary.

At slow-spreading rates, the proportion of plate separation accommodated by tectonic strain varies considerably, depending on the mode of crustal accretion. Along some ridge segments very large-offset (up to 10 km (ref. 56)) low-angle normal faults, known as detachment faults and with their uplifted footwalls termed oceanic core complexes, typically accommodate 40 to 80% of plate separation²² and up to 100% at ultraslow spreading rates⁵⁷. Between 12° 30' N and 35° N on the Mid-Atlantic Ridge, it is estimated that detachment faults occur along at least 50% of the ridge axis, where a single fault accommodates ~50% of plate separation⁵⁸. Although detachment fault surfaces are observed to be draped in talus breccias⁵⁶ and/or to produce ultramafic mass-wasting deposits²⁴, these deposits have different geometries to that depicted in Extended Data Fig. 1 and we therefore do not model their thickness using equation (14) here. To fully quantify the global ocean crustal talus breccia abundance, the geometries of the talus deposits associated with detachment faults need to be further investigated.

Along more magmatically robust slow-spreading ridge segments, fault size (that is, heave and throw) and spacing are highly variable; at spreading segment centres, faults typically have moderate offsets, whereas at spreading segment ends, the faults have greater offsets but are more widely spaced²¹. Given this inverse relationship between heave and fault spacing, the resultant total tectonic strain does not vary substantially along axis of magmatic segments of slow-spreading ridges²¹.

To explore how the variability in the geometry of non-detachment normal faults along mid-ocean ridges may impact talus breccia generation we model breccia thickness (T_B) at ridge segments spreading at slow to fast rates. Here we apply a parametric bootstrapping (Monte Carlo simulation) technique to robustly constrain the posterior probability distribution of breccia thickness at each location. We apply prior probability distributions of the discrete parameters in equation (14). To capture the variability in fault geometries at each location modelled, this requires detailed observations of the fault populations' geometries. Unfortunately, the availability of such datasets is limited.

Here we consider observations along the entire slow spreading (~26 mm yr⁻¹ full rate) segment of the Mid-Atlantic Ridge (MAR) at 29° N (ref. 21) as representative of typical axial valley morphology of slow-spreading ridges that generate non-detachment-fault seafloor. Deep-towed sidescan sonar images along this ridge segment were collected with an ~10-m spatial resolution along 0.5-km spaced east–west transects across the NNW- (O10) trending ridge axis, to constrain the geometry of faulting along the ridge segment²¹. The mean heave of all faults identified was reported to be 197 ± 293 m (1-sigma). Furthermore, for faults with $h < 500$ m, the cumulative heave-frequency distribution was found to be characterized by an exponential distribution²¹. Assuming a theoretical normal fault dip of 60° (refs. 59–61), the mean observed heave equates to mean throw of ~350 m (equation (7)). To model the average breccia thickness expected to accumulate on crust generated along this segment, fault throw is therefore designated as an exponential distribution with a mean value of 350 m, maximum of 1,700 m and minimum of 1 m based on the observed distribution of fault throws²¹. Strain is designated as a uniform distribution ranging between 10 and 15% (ref. 21). Fault dip is designated as a Gaussian distribution with a median value of 60°, a maximum dip angle of 75° and minimum dip angle of 45° based on theoretical fault dips and observed fault scarp geometries⁶². The angle of repose is designated as a uniform distribution ranging between 25 and 35°, based on slopes determined from

high-resolution bathymetry of basaltic debris deposits at 16° 38' N on the Mid-Atlantic Ridge that were consistent with the angle of repose in non-cohesive granular flow experiments²⁴. The proportion of the fault scarp covered by talus is designated as 0.6 ± 0.1 , based on observations of the proportion of the axial valley wall covered by talus deposits at 16° 38' N on the Mid-Atlantic Ridge²⁴. These prior distributions were randomly sampled and iterated 1,000,000 times over equation (14) to estimate a mean breccia thickness of 10 m, with a robustly estimated uncertainty of 8.4 m (1- σ equivalent; Extended Data Fig. 2).

To investigate the impact that the proportion of plate separation accommodated by tectonic strain has on fault geometry, and hence breccia accumulation, of non-detachment faults along slow-spreading ridges, we use the same approach to model the mean breccia thickness expected to accumulate on crust accreted along the MAR near 13° N. We use the results from near-bottom sidescan sonar/bathymetry profiler surveys of fault geometries along 24 profiles across two Mid-Atlantic Ridge segments between 13° 14' N and 13° 54' N (ref. 56), along which a greater proportion of plate separation is accommodated by tectonic strain than at 29° N, and there are several detachment faults despite a similar full-spreading rate (24.6 mm yr⁻¹). The cumulative tectonic strain within the past 1.86 Myr ranges from 25 to 30% between the detachment faults and increases to <42% at the latitudes of the detachment faults⁵⁶. Here we only model breccia accumulation on the ridge flank without detachment faults at each latitude (that is, the west flank of the MAR to the north of 13° 38' N and the east flank to the south⁵⁶). These non-detachment faults have current average heave and throw of 820 m and 177 m, respectively⁵⁶. However, the tectonic component of extension in this region resulted in significant crustal tilting⁵⁶, and their original dip of $65 \pm 12^\circ$ (ref. 56) equates to a mean pre-rotation throw of ~600 m. Given that both the strain and fault throw are higher along the MAR at 13° N than at 29° N, a greater average thickness of talus breccia is expected (Extended Data Fig. 3). Assuming the same values for the angle of repose and proportion of the fault scarp covered by talus as used to model the MAR at 29° N, our parametric bootstrapping approach yields an estimated mean breccia thickness of 87 ± 73 m (Supplementary Table 4 and Extended Data Fig. 4). This is five times thicker than our estimate of the mean breccia thickness along the MAR at 29° N, with such a thickness of breccia potentially capable of providing a sink for the full MOR outgassing flux (Fig. 4). However, we interpret this result with caution because (1) we only model breccia accumulation on the portion of non-detachment crust in this area and (2) the scale of faulting here is greater than in the area in which observations of talus geometries (angle of repose, R , and the proportion of fault scarp covered, x) are reported. Nonetheless, these results highlight the need to better constrain the variation in fault geometries, strain and the proportion of fault scarps covered by talus along slow-spreading ridges to more robustly quantify the global abundance of talus breccia on slow-spread crust.

Following the same approach, we also model the mean breccia thickness expected to accumulate on crust produced at faster-spreading ridge segments, given their observed fault population geometries and estimates of the proportion of plate separation accommodated across them by tectonic strain (Supplementary Table 4 and Extended Data Fig. 4). Although there is considerable uncertainty in our estimates of the mean breccia thickness at different ridge segments, and it is probably variable even between segments spreading at similar rates, the stark contrasts in tectonic strain and fault scale between slow- and fast-spreading ridges indicate that the volume of talus breccia they host also differs by several orders of magnitude.

Global abyssal hill mass-wasting fluxes and breccia thickness

Given the spatial variability in breccia abundance and uncertainties in our approach, we do not attempt to extrapolate our results to calculate the global average breccia thickness on ocean crust. However, here we compare the range of our average breccia thickness estimates

at different spreading rates to the global average breccia thickness that might be expected based on independent estimates of the global mass-wasting flux on fault-bounded abyssal hills⁶³. Hughes et al.⁶³ use a nonlinear topographic diffusion model, constrained with global observations of abyssal hill topography, to estimate an abyssal hill mass-wasting flux of $24\text{--}1,428 \times 10^6 \text{ m}^3 \text{ yr}^{-1}$, assuming faults dip 45° , the critical angle above which erosion occurs is 40° and volume is conserved (that is, porosity of talus = porosity of fractured bedrock). Given the current ocean crustal production rate of 3.4 km^2 per year (ref. 33), this would equate to a global average breccia thickness of $7\text{--}420 \text{ m}$. However, the calculated primary porosity of the U1557 talus deposit ($\sim 20\%$; Fig. 2) indicates that volume is not conserved and hence the estimated global mass-wasting flux would equate to a global average breccia thickness between 9 and 525 m . However, Hughes et al.³³ calculate the global abyssal hill mass-wasting flux (Q_{global} ; $\text{m}^3 \text{ yr}^{-1}$) following:

$$Q_{\text{global}} = \frac{A_{\text{ave}}}{\tau} LN \quad (15)$$

where A_{ave} is the cross-sectional area (ridge perpendicular; $4,978\text{--}22,207 \text{ m}^2$) eroded from an average height (200 m) abyssal hill, τ (in years) is the time for the hill to form, L is the global MOR length ($60,000$ to $70,000 \text{ km}$) and N is the number of actively growing hills in a 30-km -wide active fault window either side of the MOR. τ is calculated to be $20\text{--}200 \text{ ka}$, given the abyssal hill height and estimated vertical fault slip rate ($0.72\text{--}9.25 \text{ mm yr}^{-1}$) and, crucially, assuming only one fault is active at a time. On the basis of their observation that the average abyssal hill spacing, S , is 3 km , Hughes et al.³³ determine that the number of active faults at any time, N , is 20 . However, this is inconsistent with their assumption that only one fault is active, when determining τ . If more than one fault is active at a time (that is, the strain is distributed across multiple faults), it must take longer to grow each hill. Given full-spreading rates of 30 , 60 and 100 mm yr^{-1} the 60-km -wide active fault window represents 2 , 1 and 0.6 Myr of crustal accretion, respectively. Consequently, at these spreading rates, abyssal hill bounding faults should only be active for between 1 and 46% of the time they spend traversing the active fault window as the crust spreads away from the MOR. This suggests that Hughes et al.³³ have over-estimated the global abyssal hill mass-wasting flux by a factor of between 2 and 100 , depending on spreading rate, and that the average breccia thickness calculated above based on these fluxes is similarly over-estimated. Furthermore, if one is interested in the time-averaged global abyssal hill mass-wasting flux, then it is the volume of talus produced by a pair of faults (growing concurrently either side of the MOR) and the time taken to produce the crust between them and the next fault pair (dependent on fault spacing and spreading rate) that are important, rather than the time taken to grow each pair of hills:

$$\begin{aligned} Q_{\text{global}} (\text{m}^3 \text{ yr}^{-1}) &= \frac{2[\text{volume of single talus wedge of length } L (\text{m}^3)]}{[\text{spreading interval (years) between faults with spacing } S]} \\ &= 2[A_{\text{ave}}L] / \left[\frac{S}{\text{half spreading rate}} \right] \end{aligned} \quad (16)$$

Assuming the global abyssal hill range comprises 3-km -spaced hills that are 200-m high (that is, ignoring the observed variations in abyssal hill geometry with spreading rate), A_{ave}/S yields a more reliable estimate of average breccia thickness, on the order of 2 to 9 m . This range based on the cross-sectional area of eroded material modelled by Hughes et al.³³ is in good agreement with our estimates of average breccia thickness on slow- to intermediate-spreading-rate crust with fault scarps of similar average relief (Supplementary Table 4 and Extended Data Fig. 4).

Data availability

All data related to this manuscript can be found in Extended Data Figs. 1–4, Extended Data Table 1 and Supplementary Tables 1–6 and are also available along with the source data via Zenodo at <https://doi.org/10.5281/zenodo.16794553> (ref. 64).

Code availability

Our code is available from the corresponding author on reasonable request.

References

- MacLeod, C. J. et al. Life cycle of oceanic core complexes. *Earth Planet. Sci. Lett.* **287**, 333–344 (2009).
- Dick, H. J. B., Lin, J. & Schouten, H. An ultraslow-spreading class of ocean ridge. *Nature* **426**, 405–412 (2003).
- Escartin, J. et al. Central role of detachment faults in accretion of slow-spreading oceanic lithosphere. *Nature* **455**, 790–794 (2008).
- Anderson, E. M. The dynamics of faulting. *Trans. Edinburgh Geol. Soc.* **8**, 387–402 (1905).
- Collettini, C. & Sibson, R. H. Normal faults, normal friction?. *Geology* **29**, 927–930 (2001).
- Sibson, R. H. Frictional constraints on thrust, wrench and normal faults. *Nature* **249**, 542–544 (1974).
- Chen, J., Escartin, J. & Cannat, M. Fault scarps and tectonic strain in young volcanic seafloor. *Earth Planet. Sci. Lett.* **651**, 119174 (2025).
- Hughes, A., Olive, J.-A., Malatesta, L. C. & Escartin, J. Characterization of bedrock mass-wasting at fault-bound abyssal hills. *Earth Planet. Sci. Lett.* **648**, 119073 (2024).
- Coggon, R. M. et al. Dataset for ‘A Geological Carbon Cycle Sink Hosted by Ocean Crust Talus Breccias’ – Coggon et al. *Nature Geoscience*. Zenodo <https://doi.org/10.5281/zenodo.16794553> (2025).
- Melson, W. G. et al. *Initial Reports of the Deep Sea Drilling Project Vol. 45* (US Government Printing Office, 1978).
- Bougault, H. et al. *Initial Reports of the Deep Sea Drilling Project Vol. 82* (US Government Printing Office, 1985).
- Biju-Duval, B. et al. *Initial Reports of the Deep Sea Drilling Project Vol. 78A* (US Government Printing Office, 1984).
- Donnelly, T. et al. *Initial Reports of the Deep Sea Drilling Project Vols. 51, 52, 53* (US Government Printing Office, 1979).
- Alt, J. C. et al. *Proc. of the Ocean Drilling Program, Initial Reports Vol. 148* (Ocean Drilling Program, 1993).
- Leinen, M. et al. *Initial Reports of the Deep Sea Drilling Project Vol. 92* (US Government Printing Office, 1986).
- Stephen, R. A., Kasahara, J., Acton, G. D. & the ODP Leg 200 Shipboard Party. *Proc. Ocean Drilling Program, Initial Reports Vol. 200* (Ocean Drilling Program, 2003).
- Dziewonski, A., Wilkens, R. H., Firth, J. V. & the ODP Leg 136 Shipboard Party. *Proc. Ocean Drilling Program, Initial Reports Vol. 136* (Ocean Drilling Program, 1992).
- Menard, H. W. et al. *Initial Reports of the Deep Sea Drilling Project Vol. 91* (US Government Printing Office, 1987).
- Plank, T., Ludden, J. N., Escutia, C. & the ODP Leg 185 Shipboard Party. *Proc. Ocean Drilling Program, Initial Reports Vol. 185* (Ocean Drilling Program, 2000).

Acknowledgements

The samples and data used in this study were provided by the International Ocean Discovery Program (IODP). We thank *JOIDES Resolution* Captains H. Nienhuis, J. Robinson and T. Haart; Operations Superintendents S. Midgley, B. Rhinehart and K. Grigar; Offshore Installation Managers W. Lambert and M. Robinson; and the entire SIEM Offshore *JOIDES Resolution* crew and staff and the Texas A&M University technical staff onboard IODP South Atlantic

Transect Expeditions 390C, 395E, 390 and 393. We thank the *JOIDES Resolution* Science Operator for implementing Engineering Expeditions 390C and 395E during the pandemic, when international travel restrictions prevented scientists sailing, and the technical staff of Expeditions 390C and 395E led by C. Peng, A. de Loach and B. Novak for their efforts curating and analysing cores during the engineering expeditions. Thank you to J. Lewis at the University of Bristol for assistance in analysing Sr isotopic compositions and J. Lington at the University of Southampton for assistance in analysing whole rock carbon concentrations. This material is based upon work supported by the National Science Foundation (NSF) while G.L.C. was serving at NSF. Any opinion, findings and conclusions or recommendations expressed in this material are those of the authors and do not necessarily reflect the views of NSF. For the purpose of open access, the author has applied a Creative Commons attribution license (CC BY) to any Author Accepted Manuscript version arising from this submission. This research was supported by Royal Society University Research Fellowships URF\R1\180320 and URF\R\231021 to R.M.C. We acknowledge financial support from Natural Environmental Research Council UK-IODP Moratorium Awards including NE/X0001X/1 (R.M.C.), NE/X002012/1 (E.J.C.), NE/X002446/1 (L.J.C.G., R.M.C. and D.A.H.T.), NE/X00631X/1 (A.D.E. and D.A.H.T.), NE/X009440/1 (D.A.H.T.), NE/X003485/1 (T.M.B. and D.A.H.T.) and NE/X002543/1 (M.H.). C.M.L., P.D.K., J.E., J.B.S. and J.S.R. acknowledge financial support from National Science Foundation Award OCE-1450528. C.M.R. and E.A. acknowledge support from German Research Foundation IODP Priority Programme 527. E.R.E. and T.W. acknowledge financial support from National Science Foundation Award OCE-1326927 that supports management and operations of the *JOIDES Resolution* as a facility for the International Ocean Discovery Program.

Author contributions

R.M.C., E.J.C., L.J.C.G. and A.D.E. conceptualized this study and contributed equally to this work. R.M.C., D.A.H.T., J.B.S., C.M.L., G.L.C., M.H. and J.S.R. were proponents of the IODP South Atlantic

(SAT) drilling campaign. R.M.C., D.A.H.T., J.B.S., J.S.R. and G.L.C. were co-chief scientists of the SAT expeditions for which E.R.E. and T.W. were expedition project managers. E.J.C., P.D.K., R.M.C., C.M.L. and C.M.R. conducted shipboard core descriptions. L.J.C.G., R.M.C. and M.J.C. conducted the geochemical analyses. R.M.C., E.J.C., L.J.C.G., A.D.E., C.M.L., D.A.H.T. and J.E. analysed the data and discussed the implications. R.M.C., E.J.C., L.J.C.G. and A.D.E. developed the breccia abundance model. A.D.E. and R.M.C. performed the Monte Carlo modelling. R.M.C., A.D.E., E.J.C., L.J.C.G., D.A.H.T., C.M.L. and C.M.R. wrote the manuscript. R.M.C., E.J.C., L.J.C.G., A.D.E., C.M.L., D.A.H.T., J.S.R. and G.L.C. contributed to data visualization and production of figures. All authors contributed to reviewing and editing the manuscript.

Competing interests

The authors declare no competing interests.

Additional information

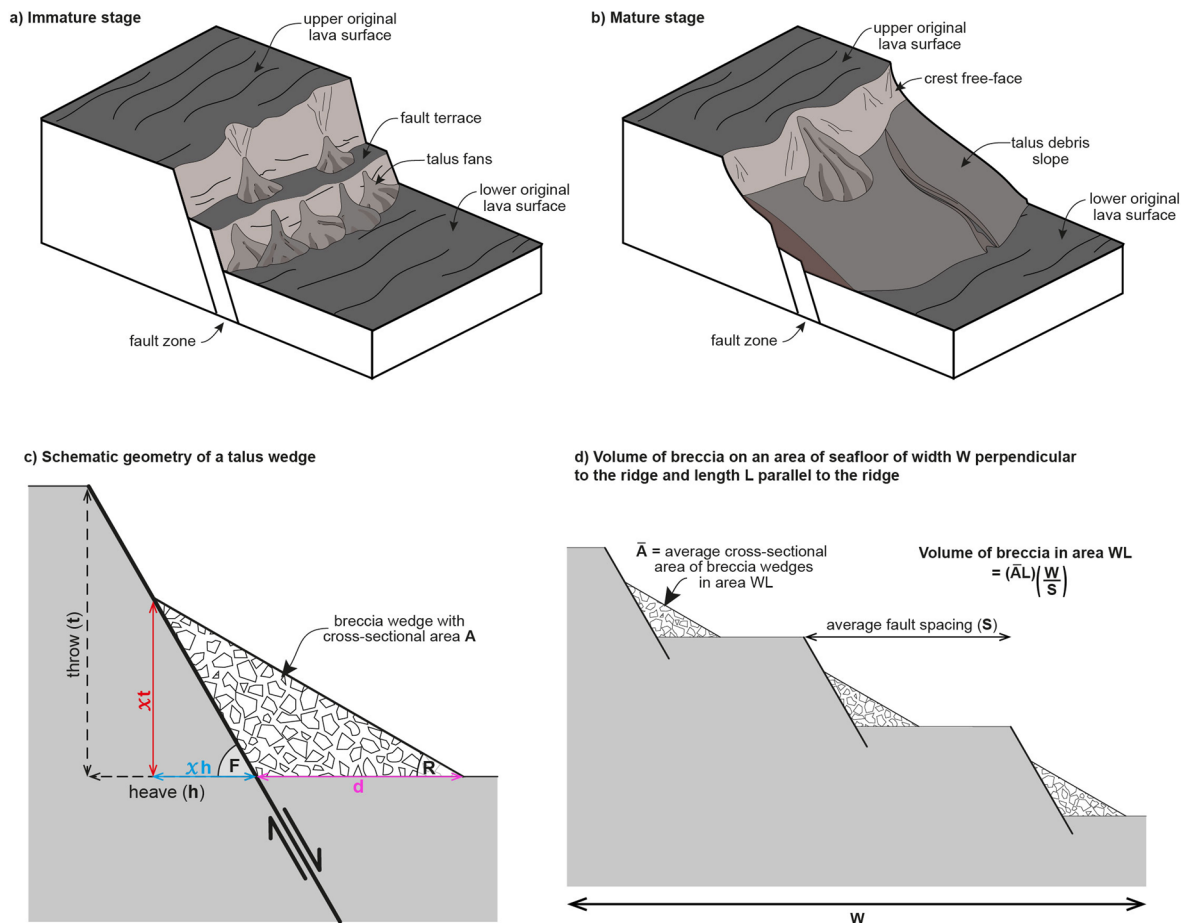
Extended data is available for this paper at <https://doi.org/10.1038/s41561-025-01839-5>.

Supplementary information The online version contains supplementary material available at <https://doi.org/10.1038/s41561-025-01839-5>.

Correspondence and requests for materials should be addressed to Rosalind M. Coggon.

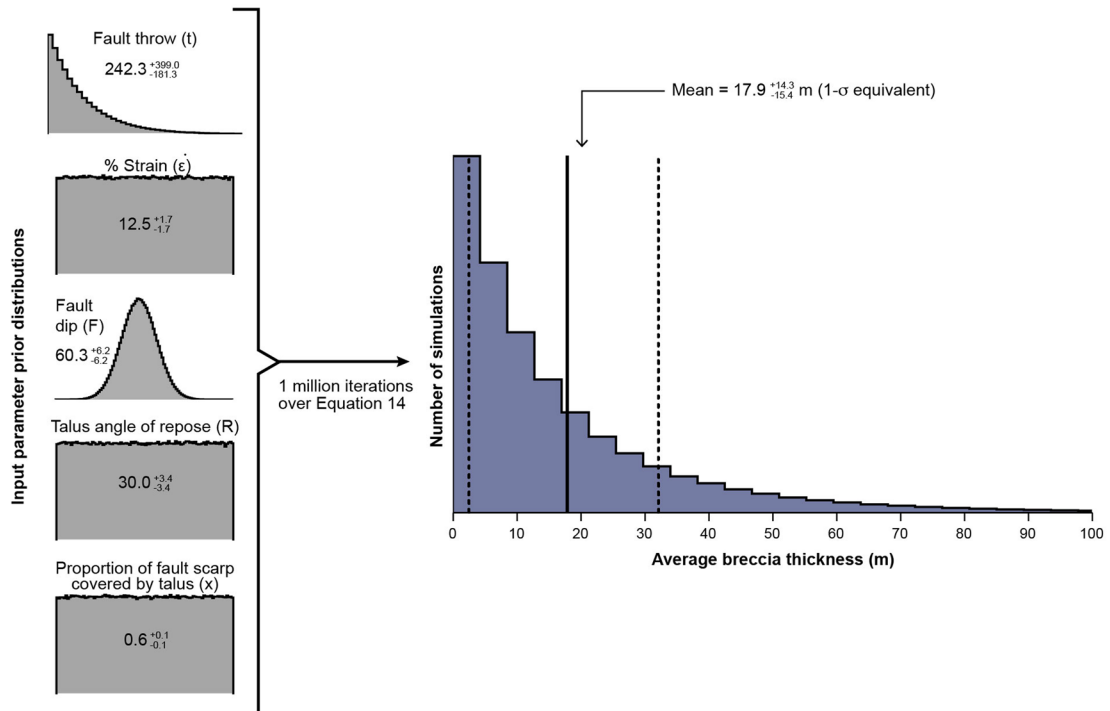
Peer review information *Nature Geoscience* thanks Andrew McCaig and the other, anonymous, reviewer(s) for their contribution to the peer review of this work. Primary Handling Editor: Alison Hunt, in collaboration with the *Nature Geoscience* team.

Reprints and permissions information is available at www.nature.com/reprints.



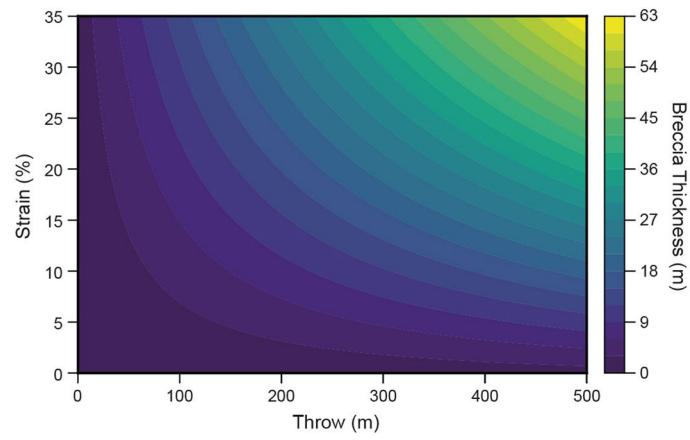
Extended Data Fig. 1 | Talus breccia geometry. The geomorphological evolution of axial valley fault scarps and their talus deposits (**a, b**), based on deep-towed sidescan sonar images of the Mid-Atlantic Ridge between 24° 00' N and 24° 40' N (modified from³⁴). **a**) Immature stage: small talus fans develop along fault terraces and the base of the fault scarp. **b**) Mature stage: a wedge of talus breccia covers the fault scarp, with its planar upper surface defined by the angle of repose of the breccia clasts. The exposed scarp (crest free-face) above the talus, is heavily eroded. **c**) The talus breccia deposits are modelled as triangular prisms parallel to the fault strike, with a triangular cross sectional area A . The fault has

throw, heave, and dip angle of t , h , and F , respectively; the breccia deposit has a planar upper surface, defined by the angle of repose (R) of the clasts, and extends a distance d (pink arrow) from the fault scarp. If the proportion of the fault scarp covered by talus is given by x , then the height of the talus wedge is xt (red arrow) and the horizontal width of the slope scarp covered by talus is xh (blue arrow). **d**) the volume of breccia on an area of seafloor with width W perpendicular to the ridge, and length L parallel to the ridge axis, depends on the average cross-sectional area of the deposits (\bar{A}), their length (L), and the number of deposits in the area (W/S , where S is the average fault spacing).

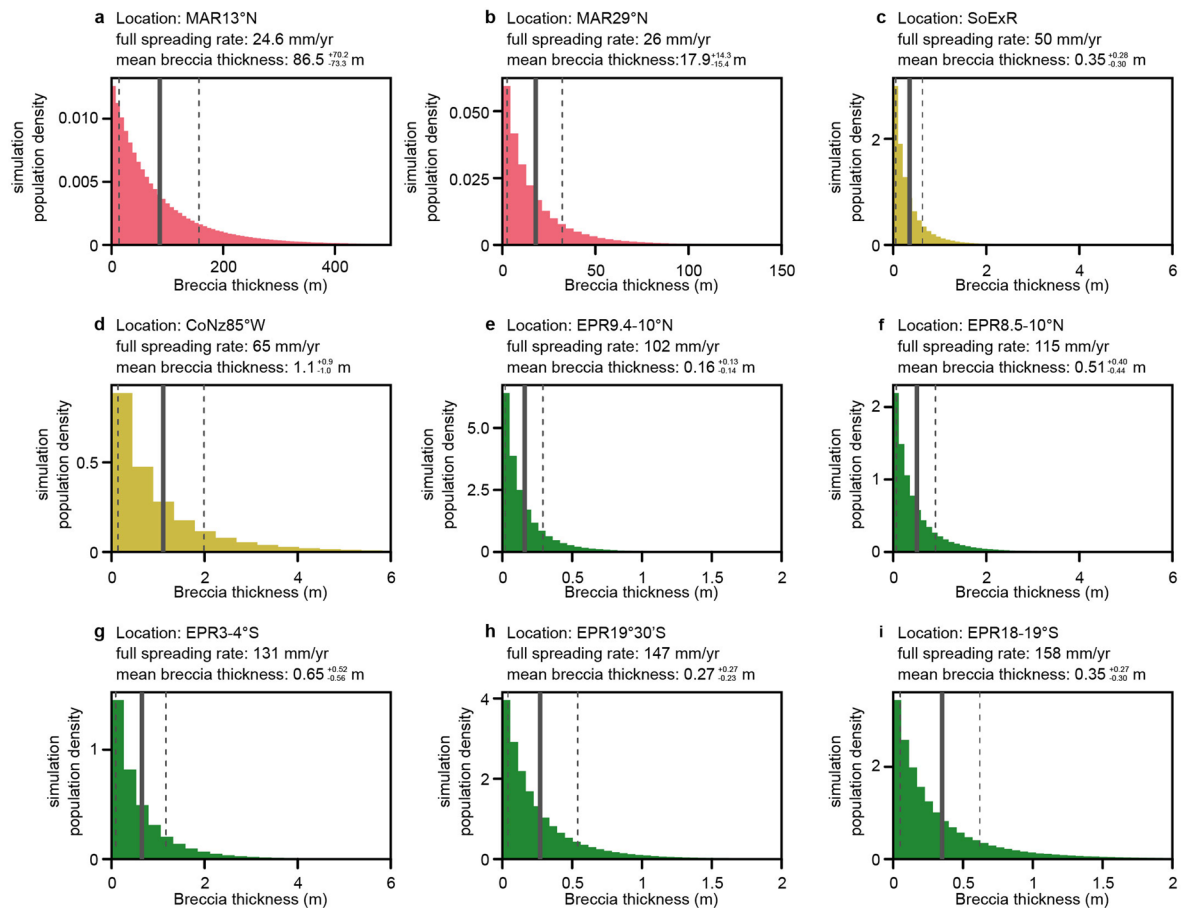


Extended Data Fig. 2 | Breccia thickness model output. Breccia thickness model output for the Mid-Atlantic Ridge 29°N area, with robustly constrained uncertainty using parametric bootstrapping (Monte Carlo simulation; mean

value with 1 σ -equivalent errors shown by solid and dashed lines, respectively). Sampled prior probability distributions of the input parameters are shown to the left and listed in Supplementary Table 4.



Extended Data Fig. 3 | Contour plot showing the dependence of breccia thickness on strain (%) and average throw. Talus breccia thickness calculated using Eq. 14, assuming constant values for the proportion of the fault scarp covered by talus (x), its angle of repose (R), and fault dip (F), of 0.6, 30° and 60°, respectively.



Extended Data Fig. 4 | Breccia thickness model outputs for ridges spreading at different rates. Breccia thickness model outputs, with robustly constrained uncertainty using parametric bootstrapping (Monte Carlo simulation) for segments of the slow-spreading Mid-Atlantic Ridge (**a,b**; red), intermediate-spreading Southern Explorer (SoExR) and Cocos-Nazca (CoNz) Ridges

(**c,d**; yellow) and fast-spreading East Pacific Rise (EPR) (**e-i**; green). Mean values with 1 σ -equivalent errors shown by solid and dashed grey lines, respectively. The sampled prior probability distributions of the input parameters, and their sources, are listed in Supplementary Table 4. Within the MAR13°N area, at each latitude, we only include faults on the ridge flank without detachment faults.

Extended Data Table 1 | Estimated bulk CO₂ contents of upper crustal sections sampled by scientific ocean drilling

Hole	Location	Crustal Age (Ma)	Spreading rate	Basement Penetration (m)	Core Recovery (%)	Bulk CO ₂ Content (wt%)	± (wt%)	CO ₂ Reference	Drill Site Reference
396B	Atlantic	13.6	Slow	255	26	0.8	0.2	(3)	(65)
556	Atlantic	17	Slow	90	50	1.9	0.3	(3)	(66)
562	Atlantic	31	Slow	178	42	2	0.3	(3)	(66)
543A	Atlantic	81	Intermediate	44	81	2.1	0.5	(3)	(67)
417A	Atlantic	120	Slow	209	61	3.9	0.2	UV (9)	(68)
417D	Atlantic	120	Slow	366.5	72	4.2	0.2	UV (9)	(68)
418A	Atlantic	120	Slow	544	72	4	0.2	UV (9)	(68)
U1557B/D	Atlantic	60.7	Slow	120	62	7	2.2 ^a	This study	(17)
504B	Pacific	6.8	Intermediate	348	34	0.2	0.1	UV (2)	(69)
896A	Pacific	6.8	Intermediate	290	27	0.5	0.2	UV (2)	(69)
597C	Pacific	28	Fast	91	53	0.4	0.1	(3)	(70)
1224F	Pacific	46	Fast	175	26	0.5	0.2	(3)	(71)
843B	Pacific	110	Fast	71	37	2.4	0.7	(2)	(72)
595B	Pacific	137	Fast	55	30	1.9	0.3	(3)	(73)
801C	Pacific	167	Fast	474	50	2.6	0.8	UV (2)	(74)

Drill Site data from refs. 65–74. ^aUncertainty is the standard deviation of the mean CO₂ content of the U1557 breccia cores, weighted by their drilled interval lengths (Methods and Supplementary Table 1). See details in CO₂ references for methods used to estimate uncertainty at other sites. UV = Upper Volcanics bulk CO₂ content reported.